Dispersion and ellipticity of Rayleigh waves in a soil substrate supporting resonant beams and plates

Jean-Jacques Marigo, Kim Pham, Agnès Maurel, Sébastien Guenneau

Dispersion and ellipticity of Rayleigh waves in a soil supporting resonant beams/plates

Jean-Jacques Marigo
Lab. de Mécanique des Solides, Ecole Polytechnique, Route de Saclay, 91120 Palaiseau, France

Kim Pham
IMSIA, CNRS, EDF, CEA, ENSTA Paris, Institut Polytechnique de Paris, 828 Bd des Maréchaux, 91732 Palaiseau, France

Agnès Maurel
Institut Langevin, ESPCI Paris, Université PSL, CNRS, 1 rue Jussieu, 75005 Paris, France

Sébastien Guenneau
The Blackett Laboratory, Department of Physics, UMI 2004 Abraham de Moivre-CNRS, Imperial College London, London SW7 2AZ, United Kingdom

The behavior of surface waves in a soil supporting an array of beams in three dimensions, or an array of plates in two dimensions, with compressional and flexural resonances is examined both theoretically and numerically. Our findings demonstrate that Love waves, characterized by displacements perpendicular to the sagittal plane, can propagate even without a homogeneous guiding layer, owing to the influence of flexural resonances in beams. Within the sagittal plane, hybridized Rayleigh waves exhibit a dispersion that is notably altered by the presence of the array, with their properties emerging from the interaction between flexural and compressional resonances. Notably, we uncover the coexistence of two Rayleigh waves with distinct wavenumbers within specific frequency ranges, corresponding to prograde and retrograde motions. Additionally, both waves significantly amplify ground motion, either horizontally or vertically. Similar physics, yet quantitatively different, is demonstrated in the case of plate arrays.

I. INTRODUCTION

Elastic surface waves can propagate within a soil substrate supporting a periodic array of resonant elements. Initial studies in this area primarily focused on this phenomenon in the GHz regime, utilizing resonant pillars typically on the scale of 1/10 micrometers [1–4]. However, when considering length scales on the order of meters, the frequency range falls within the seismic wave spectrum. In this context, a network of beams on a soil substrate serves as the idealized canonical configuration used in seismology to illustrate the "site-city interaction" problem, which was first explored in pioneering studies by [5], see also [6]. Theoretical descriptions of resonators supported by soil often rely on canonical resonant systems with one or more degrees of freedom coupled with the soil. These models typically lead to effective Robin-type boundary conditions for the soil itself [7–9]. Building upon these models, advances have demonstrated the effectiveness of seismic metasurface devices in efficiently shielding both Rayleigh waves [10–15] and Love waves [16–18]. When the specificity of the resonators, such as beam or plate-like elastic structures, was considered, only one type of resonance was initially addressed, namely compressional resonances, which were deemed more significant, as in [19], followed by flexural resonances [20–23]. Recently, the comprehensive case, including both types of resonances simultaneously, has been addressed [24], and the resulting model has been validated through comparison with simulations for scattering problems. Here, we build upon this study, extending it to analyze surface waves in the case of three-dimensional beams and two-dimensional plates, as illustrated in figure 1.

Specifically, in this study, we demonstrate that the effect of resonant structures can be encapsulated in boundary conditions linking normal stress to displacements in the soil, and these conditions involve, besides frequency, two dimensionless parameters: the slenderness of the elastic structures and a coupling parameter between these resonant structures and the soil. The resulting dispersion relations of surface waves highlight two types of waves. In the sagittal plane, we identify hybridized Rayleigh waves whose dispersion arises from the intertwined influence of flexural and compressional resonances. Particularly, in specific frequency ranges associated with flexural resonances, we show the coexistence of two Rayleigh waves. This results in soil displacements characterized by predominantly horizontal or vertical motions, indicating either high ellipticity or near-zero ellipticity. In the case of three-dimensional beams, we also demonstrate the existence of Love waves, associated with displacements perpendicular to the sagittal plane. These waves, sensitive only to flexural resonances, are the elastic counterparts of plasmon polaritons in electromagnetism [25].

The rest of the paper is organized as follows. In §II, we present the modeling. This includes a reminder of the main result obtained in [24], namely a model reduction for slender elastic structures that leads to Robin conditions applicable to the soil. We rely on this mod-

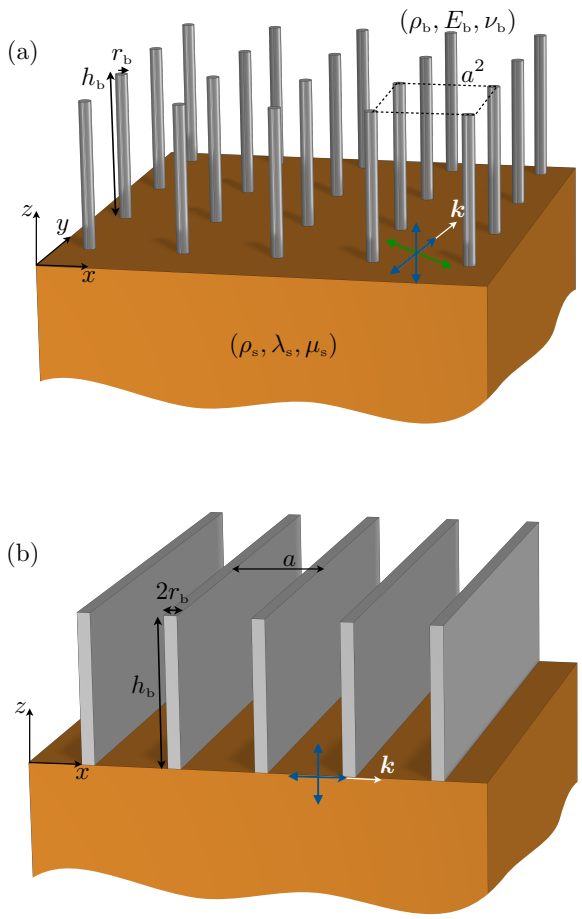

FIG. 1: Schematic views of a soil substrate supporting an array of beams in 3D (a) and of plates in 2D (b) with flexural and compressional resonances. Surface waves propagate with wavenumber in (a) $\boldsymbol{k} = (k_x, k_y, 0)$ responsible for the propagation of hybridized Rayleigh waves with sagittal-plane motions (blue arrows) and elastic SPPs with out-of-plane motions (green arrows) and in (b) $\boldsymbol{k} = (k_x, 0, 0)$ and hybridized Rayleigh waves with in-plane motions in the (x, z)-plane (blue arrows).

eling to derive the dispersion relations of hybridized Rayleigh waves and Love waves, as well as the ellipticity of Rayleigh waves. The validation of these theoretical predictions on wave numbers and associated displacements is presented in §III through comparison with results from direct numerical simulations.

II. MODELLING

This section introduces the reduced model of 3D beams that leads to effective boundary conditions applicable to the soil, namely to an elastic half-space ($z < 0$ in figure 1). The dispersion relations characterizing the propagation of surface waves are derived, along with the form of the associated displacements, enabling a prediction of the ellipticity of Rayleigh waves. In our analysis, we examine the three dimensional (3D) scenario involving an array of beams. The formulation for the two-dimensional (2D) scenario involving an array of plates is identical, owing to the definitions in Table I (additional information is provided in the Appendix A).

In the following, we denote (ρ_b, E_b, ν_b) as the mass density, Young's modulus and Poisson's ratio of the beams, respectively, and $(\rho_s, \lambda_s, \mu_s)$ as the mass density and the two Lamé's coefficients of the elastic soil substrate. The array of beams is periodic. In 3D, the unit cell has a horizontal section area of a^2, and each beam with a height h_b has a circular cross-section with a radius r_b. In 2D, the unit cell extends a, and each plate with a height of h_b has a thickness of $2r_b$.

A. Effective boundary conditions

For slender beams, as outlined in [24], it is feasible to reduce the model from three dimensions to one (vertical) dimension. This reduction yields the well-known equations

$$\begin{cases} \dfrac{\partial^4 U_\alpha}{\partial z^4} - \kappa^4 U_\alpha = 0, \quad \alpha = x, y, \\ \dfrac{\partial^2 U_z}{\partial z^2} + K^2 U_z = 0, \end{cases} \tag{1}$$

where U_α and U_z represent the displacements in the beam region and

$$\kappa = \left(\frac{4\rho_b \omega^2}{E_b r_b^2}\right)^{1/4}, \quad K = \omega\sqrt{\frac{\rho_b}{E_b}}, \tag{2}$$

are the wavenumbers associated with the flexural and compressional resonances, respectively. Equations (1) are supplemented by boundary conditions at the top of the beams and at their junction with the soil substrate. In the actual problem, stress-free boundary condition apply at the top of the beams and continuity of displacements and normal stresses apply at the beam/soil interface. In the reduced model, this leads to effective clamped-free

	slenderness $\mathcal{S}$	filling fraction θ
3D (beams)	$\mathcal{S} = 2h_b/r_b$	$\theta = \pi r_b^2/a^2$
2D (plates)	$\mathcal{S} = \sqrt{3}h_b/r_b$	$\theta = 2r_b/a$

TABLE I: Slenderness $\mathcal{S}$ and filling fraction θ for beams (3D) and plates (2D) used in the model.

boundary conditions, namely

$$\begin{cases} \text{at } z=0: \; U_\alpha = u_\alpha, \quad \dfrac{\partial U_\alpha}{\partial z} = 0, \quad U_z = u_z, \\ \qquad\qquad \sigma_{z\alpha} = -\theta E_\mathrm{b} \dfrac{r_\mathrm{b}^2}{4} \dfrac{\partial^3 U_\alpha}{\partial z^3}, \quad \sigma_{zz} = \theta E_\mathrm{b} \dfrac{\partial U_z}{\partial z}, \\ \text{at } z=h_\mathrm{b} \quad \dfrac{\partial^2 U_\alpha}{\partial z^2} = \dfrac{\partial^3 U_\alpha}{\partial z^3} = 0, \quad \dfrac{\partial U_z}{\partial z} = 0, \end{cases} \tag{3}$$

where (u_α, u_z) represent the displacements in the soil, $(\sigma_{z\alpha}, \sigma_{zz})$ denote the associated normal stress and θ is the ratio of the beam or plate cross-section to the horizontal unit cell, see Table I. It is worth noting that similar conditions can be postulated as in [21, 26] or derived using asymptotic analysis combined with homogenization [17, 18, 24] (in our case, we rely on [24]).

From (1)-(3), we can express the problem in the beam region as two decoupled problems set on U_α and U_z, each linear with respect to $u_{\alpha|z=0}$ and $u_{z|z=0}$, respectively. Specifically, denoting $\boldsymbol{r} = (x, y)$, then we have

$$\begin{aligned} U_a(\boldsymbol{r}, z) &= u_a(\boldsymbol{r}, 0) V_\mathrm{F}\left(z - h_\mathrm{b}\right), \\ U_z(\boldsymbol{r}, z) &= u_z(\boldsymbol{r}, 0) V_\mathrm{C}(z), \end{aligned} \tag{4}$$

where

$$V_\mathrm{F}(z) = V_1(\cosh \kappa z + \cos \kappa z) + V_2(\sinh \kappa z + \sin \kappa z),$$

$$V_\mathrm{C}(z) = \cos Kz + \tan Kh_\mathrm{b} \sin Kz,$$

with $V_1 = d^{-1}(\cosh \kappa h_\mathrm{b} + \cos \kappa h_\mathrm{b})$, $V_2 = d^{-1}(\sinh \kappa h_\mathrm{b} - \sin \kappa h_\mathrm{b})$ and $d = 2(1 + \cosh \kappa h_\mathrm{b} \cos \kappa h_\mathrm{b})$. Consequently, by denoting ω_0 as the characteristic resonance flexural frequency and ε as the coupling parameter defined by

$$\omega_0 = \frac{1}{\mathcal{S} h_\mathrm{b}} \sqrt{\frac{E_\mathrm{b}}{\rho_\mathrm{b}}}, \quad \varepsilon = \frac{\theta}{\mathcal{S}} \sqrt{\frac{\rho_\mathrm{b} E_\mathrm{b}}{\rho_\mathrm{S} \mu_\mathrm{S}}}, \tag{5}$$

(with $\mathcal{S}$ and θ from table I), we obtain Robin-type boundary conditions for the substrate alone in the form

$$\begin{cases} \sigma_{\alpha z}(\boldsymbol{r}, 0) = \mu_\mathrm{S} k_\mathrm{T} \varepsilon \, f_\mathrm{F}(\Omega) \, u_\alpha(\boldsymbol{r}, 0), \quad \alpha = x, y \\ \sigma_{zz}(\boldsymbol{r}, 0) = \mu_\mathrm{S} k_\mathrm{T} \varepsilon \, f_\mathrm{C}(\Omega) \, u_z(\boldsymbol{r}, 0), \end{cases} \tag{6}$$

with $k_\mathrm{T} = \omega / c_\mathrm{T}$ ($c_\mathrm{T} = \sqrt{\mu_\mathrm{S}/\rho_\mathrm{S}}$), $\Omega = \omega/\omega_0 = (\kappa h_\mathrm{b})^2$ the non-dimensional frequency and where

$$\begin{aligned} f_\mathrm{F}(\Omega) &= \sqrt{\Omega} \, \frac{\sin \sqrt{\Omega} \cosh \sqrt{\Omega} + \cos \sqrt{\Omega} \sinh \sqrt{\Omega}}{1 + \cosh \sqrt{\Omega} \cos \sqrt{\Omega}}, \\ f_\mathrm{C}(\Omega) &= \mathcal{S} \tan\left(\Omega / \mathcal{S}\right), \end{aligned} \tag{7}$$

are the impedance functions encapsulating the flexural and compressional resonances of the beams. Note that condition (6) predicts isotropic propagation in the (x, y) plane, and it is independent of the array arrangement, provided that the unit cell dimensions are subwavelength. This is a general result of homogenization models conducted at the dominant order, and it is discussed in more details in Appendix B.

Equation (6) is the important result stemming from the modeling, and we will now utilize it to characterize the surface waves supported by the soil in the presence of the array.

B. Solution for surface waves

The solution for surface waves is expressed in terms of the elastic potentials $(\varphi, \boldsymbol{\psi})$, with

$$\boldsymbol{u} = \boldsymbol{\nabla} \varphi + \boldsymbol{\nabla} \times \boldsymbol{\psi}, \tag{8}$$

and $\boldsymbol{\nabla} \cdot \boldsymbol{\psi} = 0$. By denoting $\boldsymbol{k} = k\boldsymbol{t}$, $\boldsymbol{t} = (t_x, t_y, 0)$, the (horizontal) wavevector of the surface wave, we have

$$\varphi(\boldsymbol{r}, z) = A \, e^{k\alpha_\mathrm{L} z + i\boldsymbol{k}\cdot\boldsymbol{r}}, \quad \boldsymbol{\psi}(\boldsymbol{r}, z) = \boldsymbol{B} \, e^{k\alpha_\mathrm{T} z + i\boldsymbol{k}\cdot\boldsymbol{r}}, \tag{9}$$

where the non-dimensional parameters α_L and α_T characterize the decrease in surface wave amplitudes with depth.

We express the displacements fields in the soil in terms of the components $u_\parallel = t_x u_x + t_y u_y$ in the sagital plane, and $u_\perp = -t_y u_x + t_x u_y$ perpendicular to the sagital plane. Similarly, for $\boldsymbol{B}$ in (9), we express $B_\parallel = -t_y B_x + t_x B_y$ and $B_\perp = t_x B_x + t_y B_y$. By defining

$$\beta = \frac{k_\mathrm{T}}{k}, \quad 1 - \alpha_\mathrm{T}^2 = \beta^2, \quad 1 - \alpha_\mathrm{L}^2 = \xi \beta^2, \tag{10}$$

with $\xi = \mu_\mathrm{S}/(\lambda_\mathrm{S} + 2\mu_\mathrm{S})$ $(0 \le \beta \le 1)$, we obtain

$$\begin{cases} u_\parallel(\boldsymbol{r}, z) = k \left(iA e^{k\alpha_\mathrm{L} z} - \alpha_\mathrm{T} B_\parallel e^{k\alpha_\mathrm{T} z} \right) e^{i\boldsymbol{k}\cdot\boldsymbol{r}}, \\ u_\perp(\boldsymbol{r}, z) = k \left(\alpha_\mathrm{T} B_\perp + B_z \right) e^{k\alpha_\mathrm{T} z} e^{i\boldsymbol{k}\cdot\boldsymbol{r}}, \\ u_z(\boldsymbol{r}, z) = k \left(\alpha_\mathrm{L} A e^{k\alpha_\mathrm{L} z} + iB_\parallel e^{k\alpha_\mathrm{T} z} \right) e^{i\boldsymbol{k}\cdot\boldsymbol{r}}, \end{cases} \tag{11}$$

with $(B_\perp + \alpha_\mathrm{T} B_z) = 0$. Similarly for the normal stress, with $\sigma_\parallel = t_x \sigma_{xz} + t_y \sigma_{xz}$ in the sagital plane, and $\sigma_\perp = -t_y \sigma_{xz} + t_x \sigma_{yz}$, we obtain

$$\begin{cases} \sigma_\parallel(\boldsymbol{r}, z) = \mu_\mathrm{S} k^2 \left(2i\alpha_\mathrm{L} A e^{k\alpha_\mathrm{L} z} - (1 + \alpha_\mathrm{T}^2) B_\parallel e^{k\alpha_\mathrm{T} z} \right) e^{i\boldsymbol{k}\cdot\boldsymbol{r}}, \\ \sigma_\perp(\boldsymbol{r}, z) = \mu_\mathrm{S} k^2 \alpha_\mathrm{T} \left(\alpha_\mathrm{T} B_\perp + B_z \right) e^{k\alpha_\mathrm{T} z} \, e^{i\boldsymbol{k}\cdot\boldsymbol{r}}, \\ \sigma_{zz}(\boldsymbol{r}, z) = \mu_\mathrm{S} k^2 \left((1 + \alpha_\mathrm{T}^2) A e^{k\alpha_\mathrm{L} z} + 2i\alpha_\mathrm{T} B_\parallel e^{k\alpha_\mathrm{T} z} \right) e^{i\boldsymbol{k}\cdot\boldsymbol{r}}. \end{cases} \tag{12}$$

Applying (6) with the expressions (11)-(12) yields two decoupled systems: one for the displacements in the sagittal plane $(\boldsymbol{t}, \boldsymbol{e}_z)$ and another for displacements perpendicular to the sagittal plane. Specifically, we obtain the dispersion of hybridized Rayleigh waves

$$\begin{cases} \left(1 + \alpha_\mathrm{T}^2\right)^2 - 4\alpha_\mathrm{T}\alpha_\mathrm{L} + C_\varepsilon(\beta, \Omega) = 0, \\ C_\varepsilon(\beta, \Omega) = \varepsilon\beta^3 \left[f_\mathrm{C}\alpha_\mathrm{L} + f_\mathrm{F}\alpha_\mathrm{T} \right] + \varepsilon^2 \beta^2 f_\mathrm{C} f_\mathrm{F} \left(\alpha_\mathrm{L}\alpha_\mathrm{T} - 1 \right), \end{cases} \tag{13}$$

where $(f_{\rm F}, f_{\rm C})$ are defined in (7). Note that the dispersion (13) is a unified version of that obtained in [19], where flexural resonances were neglected ($f_{\rm F}=0$), and in [24] which was restricted to the frequency range well below the first longitudinal resonance ($f_{\rm C}(\Omega)\sim\Omega$).

Displacements perpendicular to the sagittal plane, on the other hand, are associated with surface waves whose dispersion reads

$$\beta=\frac{1}{\sqrt{1+\varepsilon^2 f_{\rm F}^2(\Omega)}},\quad f_{\rm F}(\Omega)\geq 0, \tag{14}$$

representing Love-type waves but in the absence of a homogeneous guiding layer [17]. In this scenario, the guiding layer that provides classical Love waves is actually replaced by a fictitious effective layer, which is homogeneous and anisotropic, for $z\in(0,h_{\rm b})$ where (1) applies. These waves, which do not exist in the absence of beams, are the elastic analogs of electromagnetic spoof plasmons [25]. Finally, when $\epsilon=0$, we observe the retrieval of classical Rayleigh waves from (13), while Love waves disappear from (14) with $\beta=1$ hence $k=k_{\rm T}$.

In the following, we shall use that the displacement in the sagittal plane (11) take the form

$$\begin{cases} u_\parallel(\boldsymbol{r},z)=kB_\parallel\left(re^{k\alpha_{\rm L}z}-\alpha_{\rm T}e^{k\alpha_{\rm T}z}\right)e^{i\boldsymbol{k}\cdot\boldsymbol{r}},\\ u_z(\boldsymbol{r},z)=-ikB_\parallel\left(\alpha_{\rm L}re^{k\alpha_{\rm L}z}-e^{k\alpha_{\rm T}z}\right)e^{i\boldsymbol{k}\cdot\boldsymbol{r}},\end{cases} \tag{15}$$

with $r=(iA/B_\parallel)$ the real valued function of Ω

$$r=\frac{(1+\alpha_{\rm T}^2)-\varepsilon\beta\alpha_{\rm T}f_{\rm F}}{(2\alpha_{\rm L}-\varepsilon\beta\, f_{\rm F}\,)}=\frac{(2\alpha_{\rm T}-\varepsilon\beta f_{\rm C})}{(1+\alpha_{\rm T}^2)-\varepsilon\beta\alpha_{\rm L}f_{\rm C}}. \tag{16}$$

C. Ellipticity of the hybridized Rayleigh waves

We now move to an important indicator of the deleterious power of surface waves that has rarely been commented for soils supporting resonant elements. This is ellipticity χ, also called H/V because it measures the relative amplitudes of horizontal and vertical displacements induced by waves as they propagate [27]. As such, it only concerns Rayleigh waves as Love waves only produce horizontal ground shaking.

To capture the elliptical motion of displacement at ground level, ellipticity refers to the horizontal and vertical displacements in the time domain, meaning

$$\begin{cases} u_{\rm H}(\boldsymbol{r},t)=\Re\left[u_\parallel(\boldsymbol{r},0)e^{-i\omega t}\right],\\ u_{\rm V}(\boldsymbol{r},t)=\Re\left[u_z(\boldsymbol{r},0)e^{-i\omega t}\right].\end{cases} \tag{17}$$

Using (15), we obtain

$$\begin{cases} u_{\rm H}(\boldsymbol{r},t)=a\cos(\boldsymbol{k}\cdot\boldsymbol{r}-\omega(t-t_0)),\\ u_{\rm V}(\boldsymbol{r},t)=b\sin(\boldsymbol{k}\cdot\boldsymbol{r}-\omega(t-t_0)),\end{cases} \tag{18}$$

where ωt_0 is the phase of $B_\parallel$, and denoting $u_0=k|B_\parallel|$, $a=u_0(r-\alpha_{\rm T})$ and $b=u_0(\alpha_{\rm L}r-1)$, with r defined in (16), and eventually

$$\chi=\frac{\alpha_{\rm T}\beta^2+\varepsilon\beta f_{\rm C}(\alpha_{\rm L}\alpha_{\rm T}-1)}{2\alpha_{\rm L}\alpha_{\rm T}-(1+\alpha_{\rm T}^2)}=\frac{2\alpha_{\rm L}\alpha_{\rm T}-(1+\alpha_{\rm T}^2)}{\alpha_{\rm L}\beta^2+\varepsilon\beta f_{\rm F}(\alpha_{\rm L}\alpha_{\rm T}-1)}. \tag{19}$$

III. VALIDATION

In this section, we evaluate the predictive power of the model by comparing it with results obtained from direct numerical simulations conducted using Comsol Multiphysics. The physical parameters are set as follows: $E_{\rm S}=0.1$ GPa, $\rho_{\rm S}=10^3$ kg.m^{-3} and $E_{\rm b}=10E_{\rm S}$, $\rho_{\rm b}=10\rho_{\rm S}$; $\nu_{\rm S}=\nu_{\rm b}=0.3$ (hence $\xi\simeq 0.28$ resulting in a classical Rayleigh wave with $\beta=0.96$). We consider arrays of beams/plates with $r_{\rm b}=0.25$ m and $a=1$ m (for the 3D beam array, a square lattice is considered) and heights $h_{\rm b}=15$ and 30 m. The resulting parameters entering (5) are provided in Table II according to Table I.

	$h_{\rm b}=30$ m	15 m
3D	$\omega_0=0.04$ rad.s^{-1} $\varepsilon=1.3\,10^{-2},\mathcal{S}=240$	$\omega_0=0.17$ rad.s^{-1} $\varepsilon=2.6\,10^{-2},\mathcal{S}=120$
2D	$\omega_0=0.05$ rad.s^{-1} $\varepsilon=4.1\,10^{-2},\mathcal{S}=208$	$\omega_0=0.21$ rad.s^{-1} $\varepsilon=8.1\,10^{-2},\mathcal{S}=104$

TABLE II: Reference frequency ω_0 ($\Omega=\omega/\omega_0$) and dimensionless coupling parameter ε and slenderness $\mathcal{S}$ entering (6)-(7) for beams (3D) and plates (2D), see Table I.

A. Dispersions of hybridized Rayleigh waves and Love waves

To determine the dispersions of guided waves, we solve the full elastic problem numerically in 2D and in 3D within a unit cell using Bloch-Floquet conditions (we used the Solid Mechanics interface within the Acoustic module of Comsol). We consider the frequency range $\Omega\in(0,200)$, which maintains the first five flexural resonances at constant values $\Omega_n\simeq 3.5$, 22, 62, 121 and 200 ($f_{\rm F}\to\infty$ in (7)) while the frequency $\Omega=(\pi\mathcal{S}/2)$ of the first compressional resonance decreases with $h_{\rm b}$, from $\Omega=377$ to 188 in 3D and from 326 to 163 in 2D.

We begin with the case of beams in three-dimensions. Figure 2 shows dispersion branches $\beta(\Omega)$ obtained numerically (grey symbols). The results closely match the theoretical predictions for hybridized Rayleigh waves, from (13) (solid blue lines) and for Love-type waves, from (14) (dashed green lines).

As predicted by (14), the dispersion of Love waves is solely dictated by flexural resonances; in particular, the

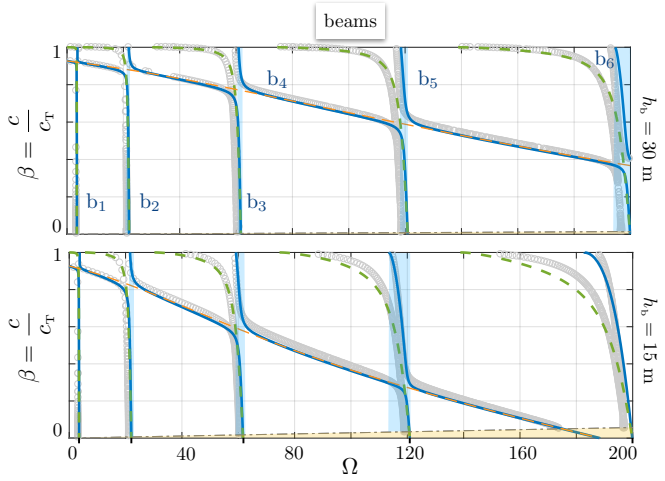

FIG. 2: Dispersion of hybridized Rayleigh waves from (13) (blue lines) and of Love waves from (14) (green dashed lines) as a function of $\Omega = \omega/\omega_0$ for beam arrays in 3D. Red dashed lines are a guide for the eye showing dispersions when flexural resonances are neglected. Gray symbols show dispersion branches obtained by direct numerical calculations (Comsol). Regions shaded blue correspond to frequency ranges where two Rayleigh wave branches coexist, those shaded red the areas outside the Brillouin zone.

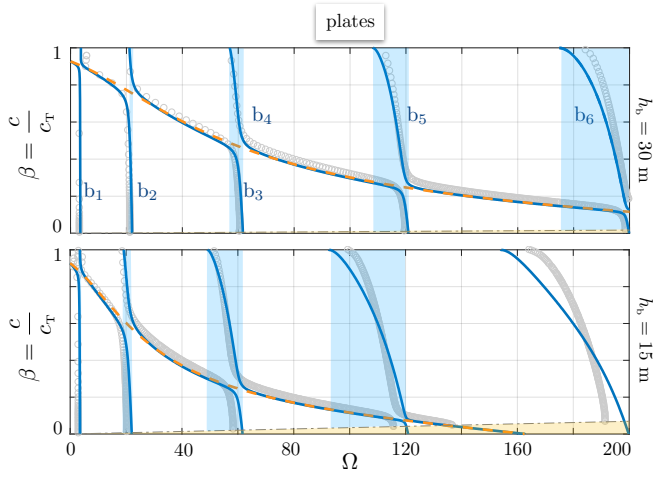

FIG. 3: Dispersion of hybridized Rayleigh wave for plate arrays in 2D – Same representation as in figure 2.

positions and thicknesses of their bandgaps, for $f_F < 0$, are independent of both the coupling parameter ε and the slenderness $\mathcal{S}$. Within the pass-bands, the dispersion varies between $\beta = 1$, meaning $k = k_T$ and the surface wave does not exist (it is a bulk wave), to very small values of β at the edge of the Brillouin zone, where $k = \pi/a$. The edge of the Brillouin $\beta = [a\omega_0/(\pi a)]\ \Omega$ is indicated by dashed-dotted black lines, and it is notable that the theory does not account for the spectrum folding due to the periodicity of the structure.

Unlike Love waves, hybridized Rayleigh waves are sensitive to both flexural and compressional resonances (the red dashed curves serve as a visual guide showing the dispersion curves when flexural resonances are neglected [19]). A notable characteristic of the observed dispersion is that each branch b_{n+1}, $n \geq 1$, begins with $\beta = 1$ slightly before the flexural resonance at Ω_n and ends with $\beta = 0$ exactly at the subsequent resonance at Ω_{n+1}. Consequently, two successive branches b_n and b_{n+1} coexist in a frequency interval just before Ω_n (indicated by shaded blue regions).

The same trends are observed for the hybridized Rayleigh waves when considering two-dimensional arrays of plates, as shown in figure 3. As one would expect, the coupling of plates to the soil is higher than that of beams for the same thickness and height (see table II). However, the slenderness $\mathcal{S}$ is slightly lower, which is also expected since plates have a higher flexural rigidity than beams. The results are displayed in figure 3. Overall agreement is good, although slightly less good than for beams, in particular at higher frequencies.

B. Rayleigh wave ellipticity

We derived the ellipticity χ using (19), accounting for Rayleigh wave dispersion given by (13). Figure 4 illustrates the variation of χ with respect to Ω for a height of $h_b = 15$ m, specifically considering beams and plates.

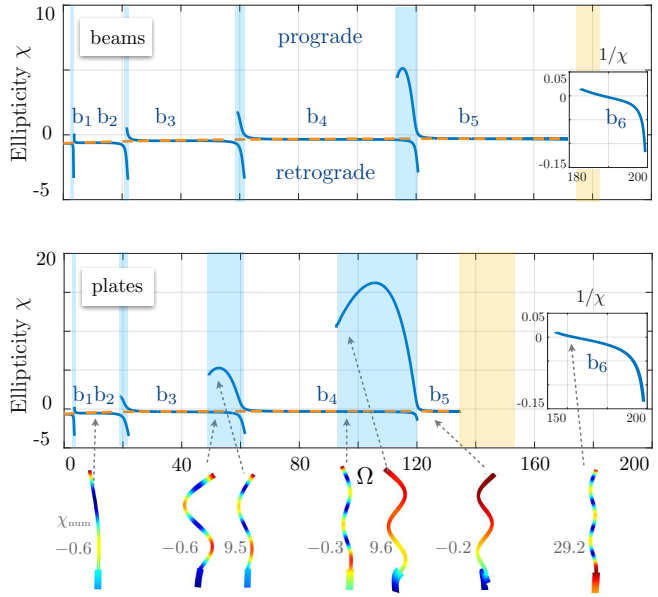

FIG. 4: Ellipticity χ of hybridized Rayleigh waves as a function of Ω for beams in 3D (top panel) and for plates in 2D (bottom panel); for the branch b_6, $1/\chi$ is shown for readibility. Blue lines show χ from (19), dashed red lines are a reference when neglecting flexion ($f_F = 0$ in (19)). The insets show the deformations in the plates, computed numerically, and the corresponding ellipticity χ_{num} (see main text).

We already note that the presence of arrays induces significant deviations from the conventional ellipticity value of -0.66 associated with classical Rayleigh waves, where β remains constant at 0.93.

Especially near flexural resonances, the soil experiences substantial horizontal shaking (high ellipticity) as well as large vertical motion (when ellipticity crosses zero), transitioning from retrograde ($\chi < 0$) to prograde ($\chi > 0$) particle motions. These transitions occur in frequency ranges where the soil supports two Rayleigh waves. Specifically, b_{n+1} exhibits peculiar ellipticity values at three typical points: (i) slightly before the resonance frequency Ω_n at the starting point $\beta = 1$ where $\chi \sim \varepsilon f_{\rm C}(\Omega_n) > 0$, whose value increases with Ω_n, hence with n; (ii) at exactly Ω_n, where particule motions change from prograde to retrograde around $\chi = 0$; here, $f_{\rm F} \to \infty$, which is consistent with (6) which predicts $u_{\rm H} = 0$ at flexural resonances, (iii) at the following resonance Ω_{n+1} (the end point $\beta = 0$) resulting in $\chi = -1/\xi < 0$ for any branch. Consequently, within the frequency range where the soil supports two Rayleigh waves, the lower branch b_n induces retrograde motions while the upper branch b_{n+1} induces prograde motions, deviating significantly from the behavior of soil without arrays.

In the same way that flexural resonances enforce $u_x = 0$ at $z = 0$, longitudinal resonances enforce $u_z = 0$. Along branch b_6 encompassing the longitudinal resonance frequency at $\Omega = 188$ in 3D and 163 in 2D, u_z typically exhibits an amplitude about 10^{-3} smaller than u_x, resulting in significant values of ellipticity. (Figure 4 depicts $1/\chi$ for b_6). It is worth noting that this branch arises from the interaction of flexural and compressional resonances, as it would not exist if flexural resonances were not considered.

These theoretical predictions regarding ellipticity are corroborated by numerical simulations of surface displacements and plate deformations, particularly within frequency ranges where two branches coexist. The results, displayed in the insets of figure 4, illustrate the plate deformations alongside the corresponding ellipticity $\chi_{\rm num}$. The qualitative agreement with equation (19) is observed, partially attributed to the presence of boundary layers at the interface between the plates and the soil. In the subsequent section, we delve deeper into a frequency range corresponding to the simultaneous existence of two branches.

C. Coexistence of two hybridized Rayleigh waves

In this section, we investigate the behavior of a classical Rayleigh wave upon encountering a region of soil supporting an array of plates, with a particular focus on the frequency range where two hybridized Rayleigh waves are expected to occur beneath the array. To achieve this, we conduct numerical experiments where the elastic substrate occupies a computational domain $\{x \in (-730, 690)\ \text{m}, z \in (-160, 0)\ \text{m}\}$ and supports plates within the range $x \in (0, 660)$ m. In the harmonic regime, at frequencies $f \in (3, 4.5)$ Hz corresponding to $\Omega \in (88.6, 132.9)$, a source positioned on the free surface at $x = -640$ m excites a Rayleigh wave, which then encounters the array at $x = 0$, as depicted in figure 5 (further details on the numerics are provided in Appendix C). There, the wave undergoes partial conversion into a bulk wave and partial conversion into surface, hybridized Rayleigh waves. Zooming in on the region of the soil beneath the array reveals the coexistence of two waves, with wavelengths λ_1 and $\lambda_2 \ll \lambda_1$.

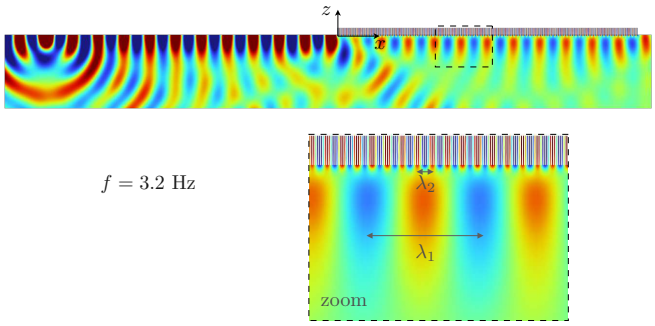

FIG. 5: Real part of the vertical displacement $u_z(x, z)$ produced by a source at $f = 3.2$ Hz, centered at $x = -640$ on the free surface. The zoom on a region in the soil below the beam array reveals the coexistence of two Rayleigh waves with wavelength λ_1 and λ_2.

To validate this observation against the model, we replicate the numerical experiments, but with the array of plates replaced by the effective boundary conditions (6) for $x \in (0, 660)$ m. The results, depicted in figure 6, demonstrate excellent qualitative agreement regarding the conversion of the classical Rayleigh wave into a bulk wave (particularly the refraction angle) and the coexistence of the two Rayleigh waves in the effective region mimicking the effect of the array of plates.

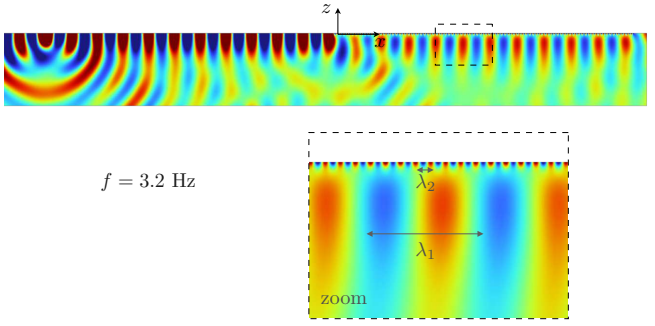

FIG. 6: Same representation as in figure 5, computed in the effective problem, where the array of plates is absent, and instead, the effective boundary conditions (6) are applied at $z = 0$ for $x \in (0, 660)$ m.

To deepen our analysis, we collect the numerical displacements recorded beneath the array. We take into

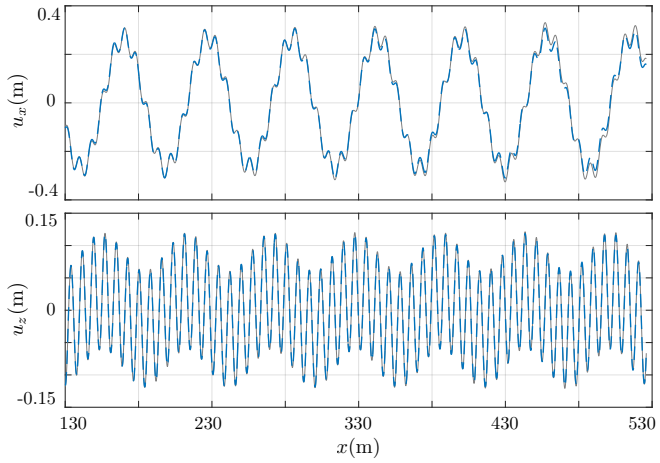

FIG. 7: Real part of u_x and u_z as a function of x at $f = 3.2$ Hz, recorded beneath the array from figure 5 (solid grey lines, $z = -2.5$ m), corresponding to the superposition of four waves with wavenumbers $\pm k_1$ and $\pm k_2$ isolated by Fourier transform (dotted blue lines).

account that the results correspond to a superposition of four waves: two right-going waves ($\boldsymbol{k}\cdot\boldsymbol{r} = kx$ in (18), with wavenumber $k = k_1, k_2 > 0$ in (18)) and two left-going waves (with wavenumber $-k$), where the left-going waves are the ones reflected at the end of the array. By Fourier transforming the complex signal, we isolate the contributions of these four waves, whose superposition is illustrated in figure 7, along with the recorded signal. Knowing these individual contributions ultimately gives us access to measurements of the ellipticity (further details can be found in Appendix C).

Figure 8 present the final results. We depict $\beta(f)$ obtained from the Floquet analysis and the corresponding ellipticity $\chi(f)$, derived from the theoretical prediction (19), using grey symbols. The blue symbols represent β and χ obtained from the data collected in the numerical experiments using the analysis described earlier. We considered $f = 3.2$ Hz illustrated in figures 5 and 7, as well as $f = 3.3$, 3.4, 3.5, 3.6 Hz, where two Rayleigh have been observed. Additionally, we examined $f = 3.7$ Hz and 4 Hz where a single Rayleigh wave is observed and $f = 4.5$ Hz confirming the presence of a band-gap.

IV. CONCLUDING REMARKS

Beams or plates on a soil substrate impact seismic wave propagation in a richer way than their acoustic counterparts. This complexity arises from the interplay between flexural and compressional resonances. In particular, (i) the dispersion of hybridized Rayleigh waves shows a significant portion of the spectrum associated with higher celerities compared to classical Rayleigh waves; (ii) these waves exhibit prograde or retrograde motion at the soil interface with significant variations in ellipticity; (iii) the existence of an out-of-plane surface wave, along with the coexistence of two Rayleigh waves in the sagittal plane within certain frequency ranges, sheds new light on the analysis of displacement components, especially for ambient noise records where horizontal displacement is the sum of the two or three contributions [28, 29]. The pillars or rods (such as trees in the META-FORET project and wind turbines in subsequent studies [23, 29]) have resonances and these resonances can then be used to interfere with incoming waves (from urban noise, railways, seismic activity, etc.) to redirect or block them.

Appendix A: Dispersion relation for the 2D case

In [24], it was shown that (1) (with $\alpha = x$) applies to a two-dimensional array of plates, where wavenumbers associated with the flexural and compressional resonances are given by

$$\kappa = \left(\frac{3\rho_\mathrm{b}\omega^2}{E_\mathrm{b}^* r_\mathrm{b}^2}\right)^{1/4}, \quad K = \omega\sqrt{\frac{\rho_\mathrm{b}}{E_\mathrm{b}^*}}, \tag{A1}$$

with $E_\mathrm{b}^* = E_\mathrm{b}/(1-\nu_\mathrm{b}^2)$, instead of (2). By performing the same calculations as in 3D, we obtain the Robin conditions (6) (with $\alpha = x$) along with (7) and the substitution $E_\mathrm{b} \to E_\mathrm{b}^*$ in (5).

Appendix B: Actual anisotropy of the propagation in the (x, y) - plane (3D case)

Here, we briefly discuss the isotropy in the (x, y) plane for the 3D model. This isotropy is evident in (6) derived

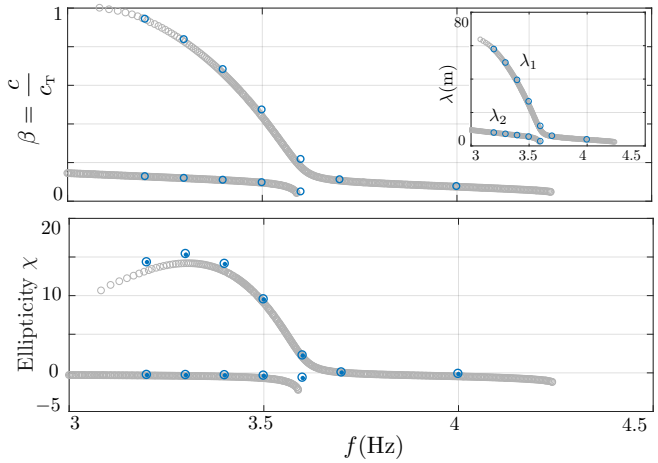

FIG. 8: Dispersion $\beta(f)$ and resulting ellipticity $\chi(f)$ of the hybridized Rayleigh waves within the frequency range $f \in (3, 4.5)$ Hz, measured using Bloch-Floquet analysis along with (19) (grey symbols as in figure 3), and deduced from the signal analysis in the numerical experiments with a source as in figure 5, see main text (open blue symbols from the right-going wave and plain blue symbols from the reflected, left-going wave).

in [24], which serves as the foundation of the present analysis. This is a general result of homogenization models conducted at the dominant order, implying that the effects of the array arrangement, which would appear at higher orders, have a relatively weak impact, see *e.g.* [17, 20, 30].

To examine the influence of the array arrangement, we consider two arrays with unit cells of the same area $a^2 = a_x a_y = 1$ m^2 (where a_x and a_y represent the lengths of the unit cell along x and y, respectively). One array is square with $a_x = a_y$, and the other is rectangular with $a_x = 3a_y$. In both cases, we solve the Bloch-Floquet problem to determine the eigenfrequencies for propagation along the direction θ_k, *i.e.*, $\boldsymbol{k} = k(\cos\theta_k, \sin\theta_k, 0)$ with $k = 0.025\pi$ and $\theta_k \in (0, 90°)$. The dispersion diagram $f(k, \theta_k = 0)$ for the square array is shown in figure 9(a) (this diagram, obtained $h_b = 15$ m, corresponds to the same data as those reported in figure 2). We select the third and fourth branches, where the frequencies corresponding to $k = 0.025\pi$ are marked by blue and red circles. Panel (b) shows the variations of these frequencies with θ_k for the two arrays. We observe a low amplitude of variation, indicating weak anisotropy. For the square array, the amplitude of variation for the two branches does not exceed 0.2%, while for the rectangular array, it reaches up to 1%, as shown in the inset where we depict a normalized relative deviation (with respect to its mean) in polar form. These results support the conclusions of the analysis in [24], indicating that the dispersion weakly depends on the array arrangement and that propagation is weakly anisotropic in the (x, y) plane.

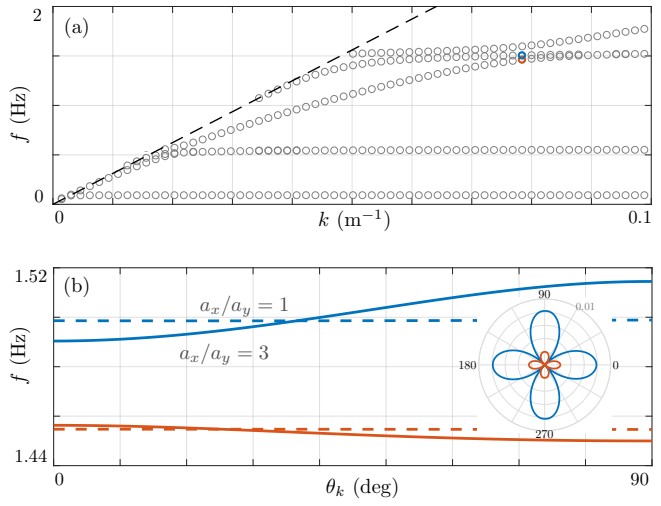

FIG. 9: (a) Dispersion diagram $f(k, \theta_k = 0)$ against k for a square array of plates with height $h_b = 15$ m (grey symbols from the same data as in figure 3); the red and blue symbols correspond to the third and fourth branches at $k = 0.025\pi$ m^{-1}. (b) Variations of $f(k = 0.025\pi$ m$^{-1}, \theta_k)$ against θ_k for the square array (dashed lines) and for the rectangular array (solid lines).

Appendix C: Additional information on the numerical experiments

The calculations are performed in the harmonic regime within a computation domain of 1420 m x 160 m along x and z, respectively (we used Comsol Multiphysics). Within the region $x \in (0, 660)$ m, plates regularly spaced with interdistance of $a = 1$ m are placed. Additionally, Perfectly Matched Layers of thickness 80 m are used at the boundaries of the domain, and a Gaussian source is imposed on the free surface $z = 0$ at $x = -640$ m in terms of a vertical traction force $\boldsymbol{\sigma} \cdot \boldsymbol{e}_z = 10^8\sqrt{50/\pi}e^{-50(x-640)^2}\boldsymbol{e}_z$, that is to say, with a lateral extension of about 1 m, a quasi point-source.

Due to the finite extent of the array, one or two hybridized Rayleigh wave are generated at $x = 0$ by the conversion of the incoming classical Rayleigh wave. These waves propagate in the soil supporting the array and are reflected at the extremity of the array at $x = 660$ m. We collect displacement signals along x at given z. To initiate our analysis, we use Fourier transform of the recorded signals. In the example shown in figure 10 for $f = 3.2$ Hz, $\pm k_1$ and $\pm k_2$, obtained from the Fourier transform

$$\hat{u}_x(K, z) = \int_0^{x_m} u_x(x, z)e^{-iKx}\mathrm{d}x. \qquad \text{(C1)}$$

We then isolate the contributions of the waves using an inverse Fourier transform filtered at the desired

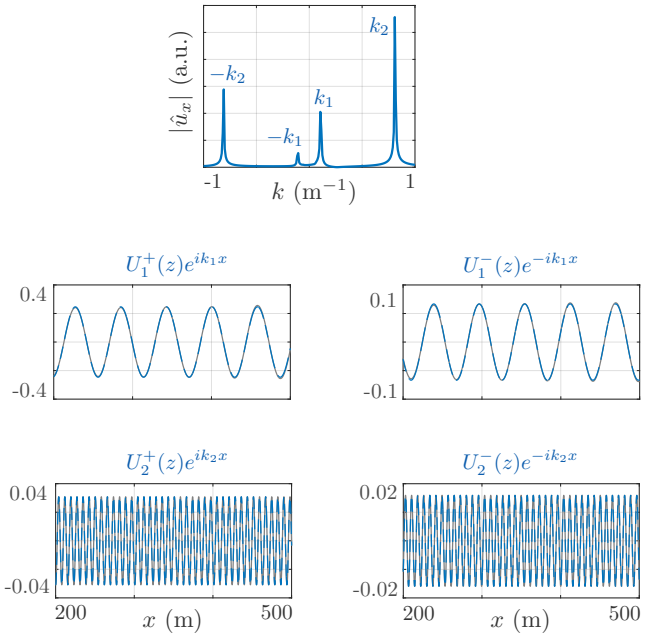

FIG. 10: Data treatment – Fourier transform of u_x measured beneath the array at $z = -2.5$ m for $f = 3.2$ Hz, as obtained from (C1). Reconstruction of the four waves using inverse Fourier transform filtered at $k = \pm k_1$ and $\pm k_2$, from (C2).

wavenumber $k = \pm k_1, \pm k_2$, as follows:

$$u^+(x,z) = \int_I \hat{u}_x(K,z) e^{-(K-k)^2/\sigma^2} e^{iKx} \mathrm{d}K, \qquad \text{(C2)}$$

the same for $w^\pm$ which denotes the inverse Fourier transform filtered at k of $\hat{u}_z$. We set $\sigma = 0.03$ m^{-1} and I as an interval of about 10σ around k. The results are exemplified in figure 10, where we report $|\hat{u}_x(k,z)|$ at $z = -2.5$ m and the resulting variations of $u_1^\pm(x,z)$ and $u_2^\pm(x,z)$ corresponding to (C2) for $k = \pm k_1$ and $\pm k_2$. The superposition of these four signals produces the fit of the collected signal, as shown in figure 7.

The Fourier transform peaks being very narrow, we approximate the fields using a single wavenumber k

$$u^\pm(x,z) = U^\pm(z) e^{\pm i|k|x}, \qquad w^\pm(\boldsymbol{r},z) = W^\pm(z) e^{\pm i|k|x}, \qquad \text{(C3)}$$

where $k = \pm k_1, \pm k_2$. Next, denoting $(A^\pm, B^\pm)$ as the complex amplitudes of the elastic potentials associated to the right- and left-going waves, we have

$$\begin{aligned} U^\pm(z) &= |k| \left(\pm i A^+ e^{|k|\alpha_\mathrm{L} z} - \alpha_\mathrm{T} B^+ e^{|k|\alpha_\mathrm{T} z} \right), \\ W^\pm(z) &= |k| \left(\alpha_\mathrm{L} A^+ e^{|k|\alpha_\mathrm{L} z} \pm i B^+ e^{|k|\alpha_\mathrm{T} z} \right), \end{aligned} \qquad \text{(C4)}$$

as seen in (11). Therefore, $(A^\pm, B^\pm)$ are deduced from the inversion

$$\begin{pmatrix} A^\pm \\ B^\pm \end{pmatrix} = \begin{pmatrix} \mp i e^{|k|\alpha_\mathrm{L} z} & -\alpha_\mathrm{T} e^{|k|\alpha_\mathrm{T} z} \\ \alpha_\mathrm{L} e^{|k|\alpha_\mathrm{L} z} & \mp i e^{|k|\alpha_\mathrm{T} z} \end{pmatrix}^{-1} \begin{pmatrix} U^\pm(z) \\ W^\pm(z) \end{pmatrix}, \qquad \text{(C5)}$$

where the result is expected to be independent of z.

Eventually, the horizontal and vertical displacements provide the ellipticity through the relation $U^\pm(0) = \pm i\chi W^\pm(0)$, see (18), yielding $\chi = \pm\left(iA^\pm - \alpha_\mathrm{T} B^\pm\right) / \left(i\alpha_\mathrm{L} A^\pm - B^\pm\right)$. At each z, we obtain two set of predictions for (χ_1, χ_2) for the right- and left-going waves, which differ by about 1%. Moreover, the results are indeed found to be indeed independent of z, with variations less than 2% when using two different values of z ($z = -2.5$ m and $z = -5$ m).

Finally, for completeness, we report the u_z displacement fields (i) in figure 11 at $f = 3.7$ Hz, where the zoom reveals a single hybridized Rayleigh wave, and (ii) in figure 12 at 4.5 Hz, revealing a band-gap that prevents the existence of any surface wave beneath the array.

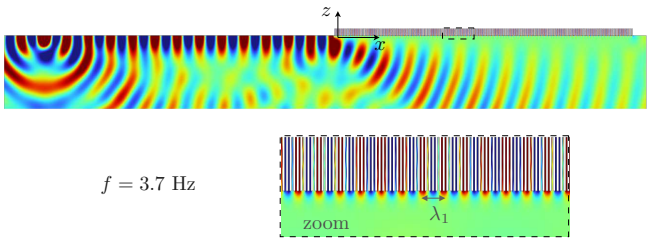

FIG. 11: Real part of the vertical displacement $u_z(x,z)$ produced by a source at $f = 3.7$ Hz, same representation as in figure 5. A single hybridized Rayleigh wave propagates beneath the beam array.

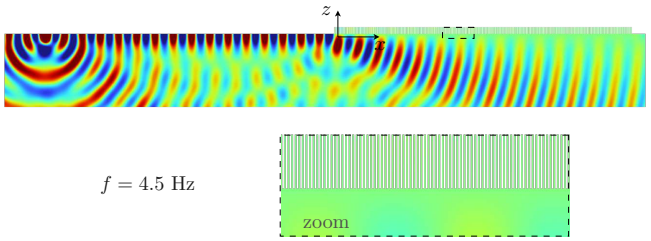

FIG. 12: Same representation as in figures 11 at $f = 4.5$ Hz, within the band-gap which prevents from the propagation of any Rayleigh wave beneath the array.

[1] A. Khelif, Y. Achaoui, S. Benchabane, V. Laude, and B. Aoubiza, Locally resonant surface acoustic wave band gaps in a two-dimensional phononic crystal of pillars on a surface, Phys. Rev. B **81**,214303 (2010).

[2] Y. Achaoui, A. Khelif, S. Benchabane, L. Robert, and V. Laude, Experimental observation of locally-resonant and Bragg band gaps for surface guided waves in a phononic crystal of pillars, Phys. Rev. B **83**, 104201 (2011).

[3] M. Oudich and M.B. Assouar, Surface acoustic wave band gaps in a diamond-based two-dimensional locally resonant phononic crystal for high frequency applications, J. Applied Phys. **111**(1) (2012).

[4] Y. Achaoui, V. Laude, S. Benchabane, and A. Khelif, Local resonances in phononic crystals and in random arrangements of pillars on a surface, J. Applied Phys. **114**(10) (2013).

[5] A. Wirgin and P.-Y. Bard, Effects of buildings on the duration and amplitude of ground motion in Mexico City, Bulletin of the Seismological Society of America **86**, 914 (1996).

[6] P. Guéguen, P. Bard, and J. Semblat, Engineering seismology: seismic hazard and risk analysis: seismic hazard analysis from soil-structure interaction to site-city interaction, in *Proc. 12th World Conference on Earthquake Engineering* (2000).

[7] E.A. Garova, A.A. Maradudin, and A.P. Mayer, Interaction of Rayleigh waves with randomly distributed oscillators on the surface, Phys. Rev. B **59**, 13291 (1999).

[8] A.A. Maznev and V.E. Gusev, Waveguiding by a locally resonant metasurface, Phys. Rev. B **92**, 115422 (2015).

[9] L. Schwan and C. Boutin, Unconventional wave reflection due to "resonant surface", Wave Motion **50**, 852 (2013).

[10] S. Brûlé, E. Javelaud, S. Enoch, and S. Guenneau, Experiments on seismic metamaterials: molding surface waves, Phys. Rev. Lett. **112**, 133901 (2014).

[11] S. Krödel, N. Thomé, and C. Daraio, Wide band-gap seismic metastructures, Extreme Mechanics Letters **4**, 111 (2015).

[12] A. Colombi, P. Roux, S. Guenneau, P. Gueguen, and R. V. Craster, Forests as a natural seismic metamaterial: Rayleigh wave bandgaps induced by local resonances, Scientific Reports **6**, 19238 (2016).

[13] A. Colombi, D. Colquitt, P. Roux, S. Guenneau, and R. V. Craster, A seismic metamaterial: The resonant metawedge, Scientific Reports **6**, 27717 (2016).

[14] A. Palermo, S. Krödel, A. Marzani, and C. Daraio, Engineered metabarrier as shield from seismic surface waves, Scientific Reports **6**, 39356 (2016).

[15] A. Colombi, V. Ageeva, R.J. Smith, A. Clare, R. Patel, M. Clark, D. Colquitt, P. Roux, S. Guenneau, and R. Craster, Enhanced sensing and conversion of ultrasonic Rayleigh waves by elastic metasurfaces, Scientific Reports, **7**(1), 6750 (2017).

[16] A. Palermo and A. Marzani, Control of Love waves by resonant metasurfaces, Scientific Reports **8**, 1 (2018).

[17] A. Maurel, J.-J. Marigo, K. Pham, and S. Guenneau, Conversion of Love waves in a forest of trees, Phys. Rev. B **98**(13), 134311 (2018).

[18] K. Pham, A. Maurel, S. Félix, and S. Guenneau, Hybridized love waves in a guiding layer supporting an array of plates with decorative endings, Materials **13**(7), 1632 (2020).

[19] D. Colquitt, A. Colombi, R. Craster, P. Roux, and S. Guenneau, Seismic metasurfaces: Sub-wavelength resonators and Rayleigh wave interaction, Journal of the Mechanics and Physics of Solids **99**, 379 (2017).

[20] J.-J. Marigo, K. Pham, A. Maurel, and S. Guenneau, Effective model for elastic waves propagating in a substrate supporting a dense array of plates/beams with flexural resonances, Journal of the Mechanics and Physics of Solids **143**, 104029 (2020).

[21] P. Wootton, J. Kaplunov, and D. Colquitt, An asymptotic hyperbolic–elliptic model for flexural-seismic metasurfaces, Proc. R. Soc. A **475**, 20190079 (2019).

[22] Y Ruan and X Liang, Reflective elastic metasurface for flexural wave based on surface impedance model, International Journal of Mechanical Sciences **212**, 106859 (2021).

[23] M. Pilz, P. Roux, S.A. Mohammed, R.F. Garcia, R. Steinmann, C. Aubert, F. Bernauer, P. Guéguen, M. Ohrnberger, and F. Cotton, Wind turbines as a metamaterial-like urban layer: an experimental investigation using a dense seismic array and complementary sensing technologies, Frontiers in Earth Science **12**, 1352027 (2024).

[24] J.-J. Marigo, K. Pham, A. Maurel, and S. Guenneau, Effective model for elastic waves in a substrate supporting an array of plates/beams with flexural and longitudinal resonances, Journal of Elasticity **146**, 143 (2021).

[25] J. Pendry, L. Martin-Moreno, and F. Garcia-Vidal, Mimicking surface plasmons with structured surfaces, Science **305**, 847 (2004).

[26] X. Pu, A. Palermo, and A. Marzani, A multiple scattering formulation for finite-size flexural metasurfaces, Proc. R. Soc. A **478**, 20210669 (2022).

[27] S. Enoch, S. Brûlé, E. Javelaud, and S. Guenneau, Flat lens effect on seismic waves propagation in the subsoil, Scientific Reports **7**, 18066 (2017).

[28] E. F. Manea, C. Michel, M. Hobiger, D. Fäh, C.O. Cioflan, and M. Radulian, Analysis of the seismic wavefield in the Moesian Platform (Bucharest area) for hazard assessment purposes, Geophysical Journal International **210**, 1609 (2017).

[29] M. Lott, P. Roux, S. Garambois, P. Guéguen, and A. Colombi, Evidence of metamaterial physics at the geophysics scale: the METAFORET experiment, Geophysical Journal International **220**, 1330 (2020).

[30] K. Pham, A. Maurel, and J.-J. Marigo, Revisiting imperfect interface laws for two-dimensional elastodynamics, Proc. R. Soc. A **477**(2245), 20200519 (2021).